

# Detection of the H92 $\alpha$ recombination line from NGC 4945

A. L. Roy<sup>1,2,3,4</sup>, T. Oosterloo<sup>5</sup>, W. M. Goss<sup>2</sup>, and K. R. Anantharamaiah<sup>3,\*</sup>

<sup>1</sup> Max-Planck-Institut für Radioastronomie, Auf dem Hügel 69, 53121 Bonn, Germany  
e-mail: aroy@mpi.fr-bonn.mpg.de

<sup>2</sup> NRAO, PO Box O, Socorro, NM 87801, USA

<sup>3</sup> Raman Research Institute, CV Raman Ave, Sadashivanagar, Bangalore 560080, India

<sup>4</sup> Australia Telescope National Facility, PO Box 76, Epping 1710, NSW, Australia

<sup>5</sup> ASTRON, PO Box 2, 7990 AA, Dwingeloo, The Netherlands

Received 21 December 2009 / Accepted 19 May 2010

## ABSTRACT

**Context.** Hydrogen ionized by young, high-mass stars in starburst galaxies radiates radio recombination lines (RRLs), whose strength can be used as a diagnostic of the ionization rate, conditions and gas dynamics in the starburst region, without problems of dust obscuration. However, the lines are weak and only few extragalactic starburst systems have been detected.

**Aims.** We aimed to increase the number of known starburst systems with detectable RRLs for detailed studies, and we used the line properties to study the gas properties and dynamics.

**Methods.** We searched for the RRLs H91 $\alpha$  and H92 $\alpha$  with rest frequencies of 8.6 GHz and 8.3 GHz in the nearby southern Seyfert galaxy NGC 4945 using the Australia Telescope Compact Array with resolution of 3". This yielded a detection from which we derived conditions in the starburst regions.

**Results.** We detected RRLs from the nucleus of NGC 4945 with a peak line strength integrated over the source of 17.8 mJy, making it the strongest extragalactic RRL emitter known at this frequency. The line and continuum emission from NGC 4945 can be matched by a model consisting of a collection of 10 to 300 H II regions with temperatures of 5000 K, densities of 10<sup>3</sup> cm<sup>-3</sup> to 10<sup>4</sup> cm<sup>-3</sup> and a total effective diameter of 2 pc to 100 pc. The Lyman continuum production rate required to maintain the ionization is 6 × 10<sup>52</sup> s<sup>-1</sup> to 3 × 10<sup>53</sup> s<sup>-1</sup>, which requires 2000 to 10 000 O5 stars to be produced in the starburst, inferring a star formation rate of 2 M<sub>⊙</sub> yr<sup>-1</sup> to 8 M<sub>⊙</sub> yr<sup>-1</sup>. We resolved the rotation curve within the central 70 pc region and this is well described by a set of rotating rings that were coplanar and edge on. We found no reason to depart from a simple flat rotation curve. The rotation speed of 120 km s<sup>-1</sup> within the central 1" (19 pc) radius infers an enclosed mass of 3 × 10<sup>7</sup> M<sub>⊙</sub>, and an average surface density with the central 19 pc of 25 000 pc<sup>-2</sup>, which exceeds the threshold gas surface density for star formation.

**Conclusions.** We discovered RRLs from NGC 4945. It is the strongest known extragalactic RRL emitter and is suited to high-quality spectroscopic study. We resolved the dynamics of the ionized gas in the central 70 pc and derived conditions and star formation rates in the ionized gas.

**Key words.** galaxies: individual: NGC 4945 – galaxies: nuclei – radio lines: galaxies

## 1. Introduction

NGC 4945 is a nearby almost edge-on spiral galaxy at a distance of (3.8 ± 0.3) Mpc (Karachentsev et al. 2007; implying a scale of 19 pc per arcsec). It has prominent dust lanes obscuring the nucleus, and is one of the brightest extragalactic sources seen by IRAS. The nuclear optical spectrum shows no sign of the Seyfert nucleus, and shows a purely starburst emission (Krabbe et al. 2001, and references therein). The presence of an active galactic nucleus (AGN) was finally settled when X-ray emission from a variable compact nuclear source was detected in the range 2 keV to 10 keV (Iwasawa et al. 1993) with heavy absorption ( $N_{\text{H}} \sim 2 \times 10^{24}$  cm<sup>-2</sup>) typical of Seyfert 2 galaxies. The absorption was predicted to be much less at higher X-ray energies, and indeed at 100 keV Done et al. (1996) found it to be the second-brightest known Seyfert galaxy in the sky. X-ray imaging by Schurch et al. (2002) with X-ray Multi-Mirror-Newton and Chandra revealed a conical plume extending 500 pc NW which they interpret as a mass-loaded superwind driven by the starburst, and they found a 6.4 keV iron K $\alpha$  line and a Compton reflection component, which are characteristic of AGNs.

A compact (<30 mas) radio core with high brightness temperature (10<sup>7</sup> K) detected by Sadler et al. (1995) at 2.3 GHz and 8.4 GHz indicates the presence of bright synchrotron emission, additional evidence for an AGN, though could possibly be radio supernovae. Mid-infrared spectroscopy was carried out with the Infrared Space Observatory by Spoon et al. (2000) to penetrate the dust obscuration, and they found no high excitation lines like [Ne V] that are common in AGNs, implying huge obscuration of  $A_{\text{V}} > 160$  assuming that a narrow-line region were present like that seen in, for example, the Circinus galaxy (which is similar in many ways to NGC 4945).

The nucleus is the source of abundant infrared and molecular emission, and optical emission line images show gas outflowing from the nucleus perpendicular to the galaxy plane. This activity originates from a composite starburst and AGN. An obscured nuclear starburst ring with diameter 50 pc is seen in Pa $\alpha$  (Marconi et al. 2000).

The molecular content of the NGC 4945 nucleus is rich and varied, producing the strongest known extragalactic molecular lines of many species. Over 80 transitions from 19 molecules have been found with single dishes, principally OH, H<sub>2</sub>O, CO, HCN, HCO<sup>+</sup>, CH<sub>3</sub>OH, but also many others

\* Deceased.

with the Swedish-ESO-Submillimetre Telescope (SEST) and Parkes from 1.6 GHz to 354 GHz (Gardner & Whiteoak 1974; Whiteoak & Gardner 1974; Whiteoak et al. 1980; Whiteoak & Wilson 1990; Whiteoak & Gardner 1986; Dos Santos & Lépine 1979; Batchelor et al. 1982; Henkel et al. 1990, 1994; Curran et al. 2001; Wang et al. 2004). Many require densities of  $10^5 \text{ cm}^{-3}$  for excitation and yield cloud temperatures of  $T_{\text{kin}} \sim 100 \text{ K}$ . Wang et al. (2004) could determine isotope ratios of C, N, O, and S, and see isotope enrichment by ejecta from massive stars relative to that of fresh gas inflowing through a bar showing that the starburst is old enough to have affected the isotopic composition of the surrounding interstellar medium. Interferometric imaging of the HNC and  $\text{HCO}^+$  molecular distributions by Cunningham & Whiteoak (2005) with the Australia Telescope Compact Array (ATCA) showed rotation of the molecular disk in the central  $6''$  with rotation speed of  $135 \text{ km s}^{-1}$ .

Imaging with very long baseline interferometry of the  $\text{H}_2\text{O}$  masers by Greenhill et al. (1997) resolved the rotation curve over the central 40 milliarcsec ( $0.7 \text{ pc}$  diameter) with a velocity range of  $\pm 150 \text{ km s}^{-1}$  inferring a central mass of  $1.4 \times 10^6 M_{\odot}$ . The rotation is in the same sense and in the same plane as the galaxy disk.

CO has been imaged at resolution from  $43''$  to  $15''$  with SEST by Dahlem et al. (1993), Ott et al. (2001), and Mauersberger et al. (1996), and interferometrically at  $4''$  with the Submillimeter Array (SMA) by Chou et al. (2007). All groups found the CO to be strongly concentrated towards the centre in a disk of molecular material  $16'' \times 11''$  ( $310 \text{ pc} \times 210 \text{ pc}$ ). Chou et al. (2007) show that the disk rotates, within the central  $5''$  ( $95 \text{ pc}$ ) radius in the plane of the galaxy disk with simple rigid-body circular rotation. At larger radius the isovelocity contours show an “S” shaped asymmetry due to a bar potential, and at the centre there is an unresolved kinematically decoupled component with a broad ( $340 \text{ km s}^{-1}$ ) velocity range. They find that this last component is a good candidate for CO emission from the obscuring AGN torus, and too dense to be part of the starburst-driven molecular outflow.

The ionized gas phase has been imaged in  $\text{H}\alpha + \text{N II}$ ,  $[\text{O III}]$ , and Bry by Moorwood & Oliva (1994), Moorwood et al. (1996) and Lípari et al. (1997) and in  $\text{Pa}\alpha$  by Marconi et al. (2000). The optical lines show a conical wind-blown cavity, and the infrared lines (Bry and  $\text{Pa}\alpha$ ) show a starburst disk at the base of the cavity extending over some  $8''$  and so are embedded within the molecular disk which extends to  $16''$ . Despite the cone resembling Seyfert ionization cones, it lacks  $[\text{O III}]$  emission and so that origin has been excluded. Spectra in  $\text{H}\alpha + \text{N II}$  show motions of  $\pm 500 \text{ km s}^{-1}$  in the cone and optical line ratios typical of low-ionization nuclear emission-line region galaxies. Infrared spectra covering Bry,  $\text{P}\beta$  and shocked molecular hydrogen by Koornneef (1993), Moorwood & Oliva (1994), and Spoon et al. (2003) resolve the nuclear rotating disk over the central  $\pm 250 \text{ pc}$ , showing a velocity range of  $500 \text{ km s}^{-1}$ . The neutral hydrogen optical emission region is within the molecular hydrogen region, with shock excitation from a nuclear wind from the central cluster. The starburst seen in Bry is powerful enough to supply the  $2 \times 10^{10} L_{\odot}$  radiated in the infrared.

The ionized gas component can also be imaged using radio recombination lines (RRLs), which are not affected by extinction unlike at optical and near-infrared wavelengths. In this paper we describe RRL imaging of the nucleus of NGC 4945 in which we detect  $\text{H}92\alpha$  emission and resolve the rotation curve. RRLs have been used to derive mass, density and ionizing photon fluxes for the ionized gas in other galaxies, from which star formation

rates have been derived. The diagnostic methods are described by Anantharamaiah et al. (2000, and references therein), and in detail by Mohan (2002). The mere detection of RRL emission requires the presence of thousands of H II regions or of stimulated emission since a single H II region like the Orion nebula placed at that distance would be undetectably weak.

There are now 15 known extragalactic RRL detections (including NGC 4945), all in bright starburst galaxies, which are listed by Roy et al. (2008). Most of those detections resulted from improving the search sensitivity by a factor of ten during the 1990s and by making surveys of promising bright candidates using the Very Large Array (VLA) and ATCA. Our observation of NGC 4945 reported here was the third detection made in our ATCA survey for  $\text{H}92\alpha$  emission. The other two detections from this survey (NGC 3256 and the Circinus galaxy) were reported by Roy et al. (2005, and 2008). NGC 4945 has proven to be the strongest known extragalactic RRL emitter on the sky.

We give velocities in the heliocentric frame using the optical velocity definition throughout this paper.

## 2. Observations

We observed NGC 4945 with the ATCA simultaneously in the lines  $\text{H}91\alpha$  and  $\text{H}92\alpha$  with two orthogonal linear polarizations. The observing parameters and results are summarized in Table 1.

Calibration and imaging were done using the AIPS software using standard methods. The flux-density scale assumed that PKS B1934-638 had a flux density of 2.99 Jy at 8295 MHz and 2.87 Jy at 8570 MHz, based on the Baars et al. (1977) flux-density scale. A phase calibrator was observed every half hour to correct the instrumental phase response. A bandpass calibrator was observed every few hours for correcting the instrumental frequency response (bandpass). Phase corrections obtained from self calibration of the continuum source were applied to the spectral line data. Continuum emission was subtracted from the line data using the method UVLSF (Cornwell et al. 1992) in which the continuum is determined for each baseline by a linear fit to the spectrum. The final continuum and line images were made using natural weighting of the  $(u, v)$  data to achieve maximum possible signal-to-noise ratio.

Uncertainties on the flux densities have an 11% rms random multiplicative component due to flux-density bootstrapping and atmospheric opacity, a 0.21 mJy rms random additive component due to thermal noise in a 1 MHz channel and a systematic multiplicative component of 11% rms due mainly to the uncertainty in the Baars et al. flux-density scale.

## 3. Results

The ATCA continuum and line images, and integrated spectrum are shown in Fig. 1, and the velocity field and position-velocity diagram are shown in Fig. 2.

The continuum image shows a well resolved structure extended along the plane of the galaxy in position angle  $47^\circ$ . Line emission was detected from the nuclear region with a well resolved structure that is extended along the plane of the galaxy like the continuum, though more compact and clumpy than the continuum emission. The line emitting region has a total deconvolved extent of  $8.1'' \times 1.7''$  ( $150 \text{ pc} \times 30 \text{ pc}$ ). The peak of line emission is coincident with the peak of continuum emission within  $1''$ . The total area of line emission is 1.5 times the naturally-weighted beam area (8.6 times the uniformly-weighted beam area), or  $4500 \text{ pc}^2$ . The  $\text{H}91\alpha + \text{H}92\alpha$  spectrum integrated

**Table 1.** ATCA Observational Parameters and Results for NGC 4945.

NGC 4945	
Array configuration	750D (1993 Jul. 25), 1.5D (1994 Sep. 21), 6C (94 Oct. 03)
Date of observation	1993 Jul. 25, 1994 Sep. 21, 94 Oct. 03
Integration time	22.7 h
Transitions	H92 $\alpha$ & H91 $\alpha$
$\nu_{\text{rest}}$ of RRL	8309.38 MHz & 8584.82 MHz
$\nu_{\text{band-centre}}$	8295.00 MHz & 8570.00 MHz
$V_{\text{systemic, helio, optical}}$	560 km s $^{-1}$ (Paglione 1997)
Distance	3.8 Mpc
Bandwidth, channels, IFs	64 MHz, 64, 4
Spectral resolution	36 km s $^{-1}$
Minimum baseline	0.86 $k\lambda$
Beam size (natural weight)	3.4'' $\times$ 2.7'' at $-55^\circ$
Beam size (uniform weight)	1.35'' $\times$ 1.18'' at $-4^\circ$
Phase calibrator (B1950)	1320-446
Bandpass calibrator (B1950)	1226+023, 1320-446, 1934-638, 2251+158
<b>Line and Continuum Properties</b>	
Peak continuum flux density	(538 $\pm$ 80) mJy beam $^{-1}$ (natural weighting)
Total continuum flux density	(1424 $\pm$ 220) mJy
Noise per image channel	0.21 mJy beam $^{-1}$
Peak line flux density	(17.8 $\pm$ 2.8) mJy
Integrated line flux	(11.3 $\pm$ 1.8) $\times 10^{-22}$ W m $^{-2}$
Measured line width ( <i>FWHM</i> )	(225 $\pm$ 15) km s $^{-1}$
Deconvolved line width ( <i>FWHM</i> )	(221 $\pm$ 15) km s $^{-1}$
Centroid helio. optical vel.	(581 $\pm$ 15) km s $^{-1}$
No. of beam areas where line is observed	1.5 (naturally weighted)

over the line emitting region shows a strong line detection with significance of  $52\sigma$ , with centroid at 581 km s $^{-1}$  in good agreement with the CO systemic velocity of 585 km s $^{-1}$  (Chou et al. 2007) and with the velocity of the HI absorption towards the nucleus of 585 km s $^{-1}$ , though significantly higher than the HI systemic velocity inferred from the whole galaxy of 557 km s $^{-1}$  (Ott et al. 2001). The line *FWHM* is 220 km s $^{-1}$  after deconvolving the instrumental velocity resolution of 42 km s $^{-1}$ .

The position-velocity diagram (Fig. 2) shows a well resolved symmetric structure indicating undisturbed rotation with a flat rotation curve extending in close to the nucleus. The rotation curve is modelled in Sect. 5.

#### 4. Modelling line formation in the ionized gas

Two types of models have been considered for the RRL emission from the nuclei of external galaxies: one based on a uniform slab of ionized gas and the other based on a collection of compact H II regions. Such models have been discussed by Anantharamaiah et al. (2000, and references therein), and are documented in detail by Mohan (2002). These models take as constraints the integrated RRL strength at one or more frequencies, the radio continuum spectrum, and the geometry of the line emitting region.

For modelling the RRL emission from NGC 4945 we used the integrated line strength (17.8 mJy), line width (280 km s $^{-1}$ ), size of the line-emitting region (equivalent to a 70 pc diameter sphere), continuum emission (1424 mJy), and spectral index ( $-0.75$ ) to constrain conditions in the ionized gas. Using the collection of H II regions model, models with 10 to 300 H II regions, all with  $T_e \sim 5000$  K,  $n_e \sim 10^3$  cm $^{-3}$  to  $10^4$  cm $^{-3}$  and a total effective diameter of the line-emitting gas of 2 pc to 100 pc produced good matches to the line and continuum emission. Parameters derived for typical allowed models are given in Table 2.

**Table 2.** Derived properties for NGC 4945, using model results for  $T_e = 5000$  K.

NGC 4945	
Electron temperature	5000 K
Electron density	1000 cm $^{-3}$ to 10 000 cm $^{-3}$
Effective size <sup>a</sup>	2 pc to 100 pc
Total ionized gas mass	(2 to 6) $\times 10^5 M_\odot$
$N_{\text{LyC}}$	$6 \times 10^{52}$ s $^{-1}$ to $3 \times 10^{53}$ s $^{-1}$
No. O5 stars	2000 to 10 000

**Notes.** <sup>(a)</sup> The total size, i.e. (total volume of all H II regions)<sup>1/3</sup>.

The range of possible filling factors can be estimated by comparing the total volume of the line-emitting gas (8 pc $^3$  to  $1 \times 10^6$  pc $^3$  derived from the total effective diameter) to the volume of the line-emitting region ( $5.3 \times 10^5$  pc $^3$ , assuming cylindrical geometry with diameter of 150 pc and height of 30 pc). The range of possible values is then  $2 \times 10^{-5}$  to 1.

The inferred mass of ionized gas is  $2 \times 10^5 M_\odot$  to  $6 \times 10^5 M_\odot$ , depending on the model conditions, which requires a Lyman continuum flux of  $6 \times 10^{52}$  s $^{-1}$  to  $3 \times 10^{53}$  s $^{-1}$  to maintain the ionization. This flux is equivalent to the Lyman continuum output of 2000 to 10 000 stars of type O5, which infers a star-formation rate of  $2 M_\odot$  yr $^{-1}$  to  $8 M_\odot$  yr $^{-1}$  when averaged over the lifetime of OB stars.

This can be compared to star formation rates derived from other indicators following Hopkins et al. (2003). Taking the peak 1.4 GHz flux density of 4.0 Jy beam $^{-1}$  in the 30''  $\times$  18'' beam of the ATCA at the nucleus of NGC 4945 (Elmoultie et al. 1997) yields a 1.4 GHz luminosity of  $7.0 \times 10^{21}$  W m $^{-2}$  and a corresponding star formation rate of  $3.9 M_\odot$  yr $^{-1}$ . This can be attributed to the central 1.8'' (30 pc) diameter region following the argument of Elmoultie et al. (1997) based on the high resolution 8.4 GHz image. The IRAS 60  $\mu$ m and 100  $\mu$ m flux densities yield a far-infrared (FIR) star formation rate of  $4.1 M_\odot$  yr $^{-1}$ .

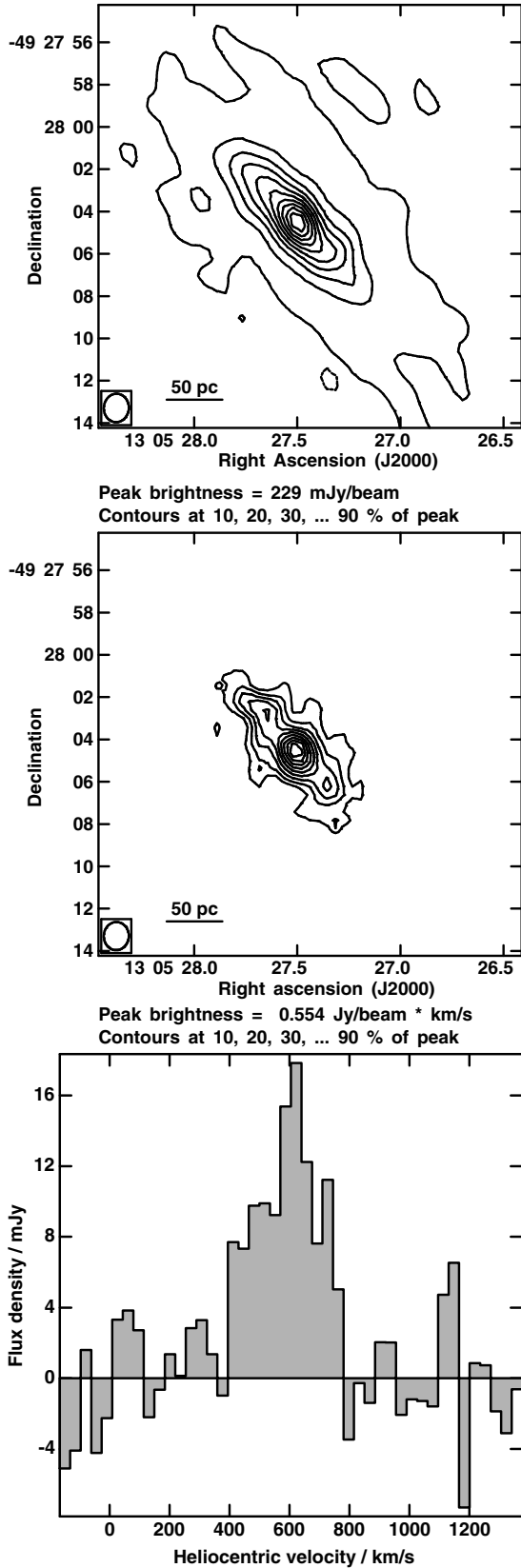


**Fig. 1.** *Top:* ATCA 8.3 GHz + 8.6 GHz continuum image with uniform weight of NGC 4945. *Middle:* ATCA uniformly weighted zeroth-moment image of H91α + H92α emission after continuum subtraction. Beamsize is 1.4" × 1.2". *Bottom:* ATCA H91α + H92α line profile integrated over the line-emitting region in the zeroth-moment image. Rms noise is 0.16 mJy beam<sup>-1</sup> channel<sup>-1</sup> and the channel width is 36 km s<sup>-1</sup>. The region of integration is a box of size 10.0" × 10.4" centred on RA 13 05 27.48 dec -49 28 04.0.

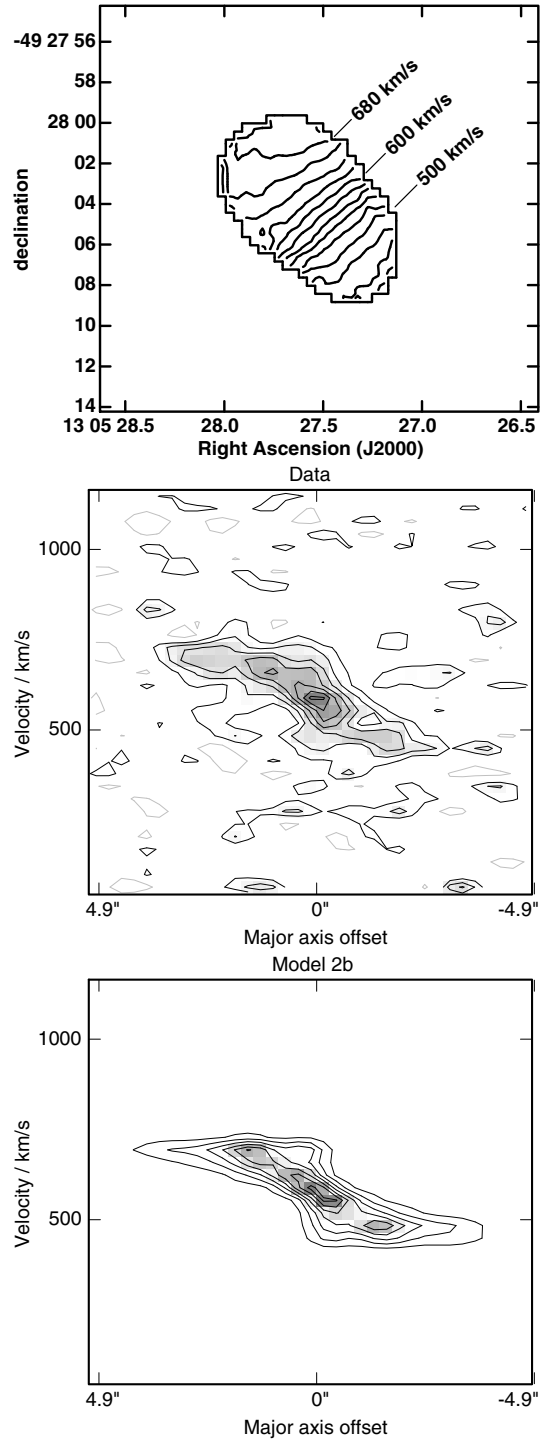


**Fig. 2.** *Top:* ATCA first-moment image of H91α + H92α emission showing rotation. Beamsize is 1.4" × 1.2". *Middle:* H91α + H92α rotation curve along the major axis of the line-emitting region (PA = 47°). Resolution is 1.3" × 36 km s<sup>-1</sup>. *Bottom:* rotation curve from the best-fit dynamical model described in Sect. 5.

These estimates agree well with the star formation rate estimated from the RRL emission of 2 M<sub>⊙</sub> yr<sup>-1</sup> to 8 M<sub>⊙</sub> yr<sup>-1</sup>. The Hα and U-band-based star formation rates were not estimated due to the extreme absorption in the optical band. The supernova rate estimated by Forbes & Norris (1998) from the 4.8 GHz flux density is 0.23 yr<sup>-1</sup>, and from the [Fe II] flux is much lower at 0.005 yr<sup>-1</sup>. These can be converted into star-formation rates following Fukugita & Kawasaki (2003), yielding rates of

$19 M_{\odot} \text{ yr}^{-1}$  and  $0.4 M_{\odot} \text{ yr}^{-1}$ . These bracket the range we estimated from the RRL emission.

Our RRL-based SFR estimate assumed no dust absorption between the OB stars and the H II regions producing the RRL emission. The effect of dust can be estimated by comparing the bolometric luminosity ( $L_{\text{bol-RRL}}$ ) from the stellar population needed to ionize the RRL-emitting gas to the observed FIR output ( $L_{\text{FIR}}$ ) from the region. If ionizing photons are absorbed by dust before causing ionization, then  $L_{\text{bol-RRL}}$  will be less than  $L_{\text{FIR}}$ . The ratio  $L_{\text{bol-RRL}}/L_{\text{FIR}}$  thus gives the ratio of the number of photons absorbed by the gas to the number of photons absorbed by the dust. We derived  $L_{\text{bol-RRL}}$  by taking our RRL-based  $L_{\text{LYC}}$  and dividing by the  $L_{\text{LYC}}/L_{\text{bol}}$  ratio of 0.29 calculated for a stellar population with Salpeter IMF, lower-mass cutoff of  $1 M_{\odot}$  and upper-mass cutoff of  $87 M_{\odot}$ , and using the mass-luminosity relation for OB stars in Table 5 of Vacca et al. (1996). This resulted in  $L_{\text{bol-RRL}} = 1.2 \times 10^9 L_{\odot}$  to  $5.7 \times 10^9 L_{\odot}$ , compared to  $L_{\text{FIR}}$  from region of  $1.6 \times 10^{10} L_{\odot}$  (Brock et al. 1988). The ratio  $L_{\text{bol-RRL}}/L_{\text{FIR}}$  shows that the gas volume in the nuclear region is illuminated by ionizing radiation that represents only 7.5% to 35% of the ionizing flux from the stars needed to power the FIR output; the rest, we assume, is absorbed by dust within the H II regions. Converting to opacity using Fig. 2 of Petrosian (1972) yields dust opacities of 1.3 neper to 3.4 neper within the H II regions.

Given so much absorption, it is unexpected that the star-formation rate inferred from the RRL emission, which assumed zero absorption, should agree so well with that inferred from  $L_{\text{FIR}}$ . An important assumption made while deriving the RRL-based star formation rate from the present inferred number of OB stars was that the stars are being formed at a steady rate that would maintain the present numbers.

## 5. Dynamical modelling of the ionized gas

We used the rotation curve to constrain the gas kinematics by fitting to the data a simple model consisting of a set of rings, coplanar, edge-on, with an initially flat rotation curve. The brightness of each ring was determined by deprojecting the observed zeroth-moment image to derive the radial distribution of the line intensity. The radial distribution showed a central peak and a ring of emission  $2.5''$  (50 pc) from the nucleus.

We refined the model iteratively, varying the systemic velocity, rotation velocity, and velocity dispersion until we achieved a reasonably close match to the data, and found no reason to depart from a simple flat rotation curve. The biggest residual between the model and data was at the nucleus and a smaller one at the 50 pc ring. To improve the model, we refined the radial profile of line emission strength at the nucleus and the ring. The data required us to boost the central peak to 25 times the brightness of the more extended emission and to place that gas at the systemic velocity. This could correspond to gas on circular orbits moving transverse to the line of sight in front of the nucleus. The data also required us to put half that strength in the innermost ring ( $0.4'' = 7.6$  pc) with our best-fit rotation velocity. For the 50 pc ring, we tweaked the radius and brightness. The result was a very good match to the observed data, with residuals at 1.5 times the rms noise in the position-velocity diagram.

The final model had a flat rotation curve with  $v_{\text{systemic}} = 581 \text{ km s}^{-1}$ ,  $v_{\text{rotation}} = 120 \text{ km s}^{-1}$ , and  $v_{\text{dispersion}} = 15 \text{ km s}^{-1}$ . We did not need to invoke a bar or radial motion, though the data do not strongly exclude either.

The rotation velocity of  $120 \text{ km s}^{-1}$  within the central  $1''$  (19 pc) radius infers an enclosed mass of  $3 \times 10^7 M_{\odot}$ . The

water masers (Greenhill et al. 1997) infer an enclosed mass of  $1 \times 10^6 M_{\odot}$  within 0.3 pc radius, and so most of the  $3 \times 10^7 M_{\odot}$  is extended between 0.3 pc and 19 pc radius of the nucleus. The average surface density within the central 19 pc is  $25\,000 M_{\odot} \text{ pc}^{-2}$ , which exceeds the threshold gas surface density for star-formation of  $(3 \text{ to } 10) M_{\odot} \text{ pc}^{-2}$  (Kennicutt 1989) by four orders of magnitude.

The 50 pc ring might be a Lindblad resonance, which would infer a bar and then our assumption of pure rotation would become invalid. The ring and nucleus may be seen also in CO spectra (Whiteoak & Wilson 1990; Dahlem et al. 1993), and in OH absorption (Whiteoak & Wilson 1990).

The RRL emission contains a bright peak on the nucleus at the systemic velocity. The continuum emission is smooth and does not show a similar peak and so we speculate that this might be stimulated emission along the line of sight for which the gas velocity is transverse to the line of sight and so has a long maser gain path.

## 6. Comparison with literature

H I kinematics were studied by Ott et al. (2001) with the ATCA at  $3.5''$  resolution. They saw HI in emission over the disk, with an extent of  $22' \times 4'$  ( $43 \text{ kpc} \times 7.8 \text{ kpc}$ ) and in absorption towards the nuclear continuum emission. They see an asymmetry in the large-scale H I rotation field, which they argue is due to the bar potential. The H I absorption towards the nucleus shows a uniform velocity gradient across the nucleus indicating solid-body rotation peaking at  $\pm 100 \text{ km s}^{-1}$  either side of the systemic velocity out to  $\pm 5''$  either side of the centre, with a sign of flattening beyond  $\pm 5''$  to  $\pm 7''$ . For comparison, our H91 $\alpha$  + H92 $\alpha$  rotation curve remained flat at  $\pm 120 \text{ km s}^{-1}$  either side of systemic all the way into the central  $1''$ . This difference could be due to the two-times lower spatial resolution of the HI observation compared to that of the H91 $\alpha$  + H92 $\alpha$  observation ( $3.5''$  compared to  $1.4''$ ). Were we to smooth our position-velocity diagram, or had the noise in our position-velocity diagram been a little higher, the small wings that indicate a flat rotation curve would be less visible, giving the impression of solid-body rotation. Also, in edge-on systems with a flat rotation curve, one finds the density distribution often gives the appearance of solid-body rotation.

Rotation of the larger-scale disk ( $> \pm 100''$ ) derived from CO(1–0) observations with SEST by Dahlem et al. (1993) at  $43''$  resolution shows evidence for gas inflow that is consistent with the inflow model proposed by Ables et al. (1987) from H I. This was seen also in CO(2–1) by Ott et al. (2001) with SEST at  $23''$  resolution. However, inflow was not seen in the H91 $\alpha$  + H92 $\alpha$  dynamics within  $4''$  of the nucleus.

Isovelocity contours of CO by Chou et al. (2007) show an S-shaped asymmetry due to a bar potential at distances larger than  $5''$  from the nucleus, and show simple circular rotation within that radius. The isovelocity contours of the H91 $\alpha$  + H92 $\alpha$  radio recombination line from the ionized gas component seen within  $4''$  radius of the nucleus likewise shows simple circular rotation with no asymmetry, consistent with the CO on that scale.

The rotation of the nuclear disk derived from CO(3–2) observations with SEST by Mauersberger et al. (1996) with  $15''$  resolution and with SMA by Chou et al. (2007) at  $\sim 4''$  resolution show that within  $\pm 5''$  of the nucleus, the velocity changes from  $390 \text{ km s}^{-1}$  to  $730 \text{ km s}^{-1}$ , which is broader than the velocity range of the H91 $\alpha$  + H92 $\alpha$  emission ( $460 \text{ km s}^{-1}$  to  $700 \text{ km s}^{-1}$ ) over the same region.

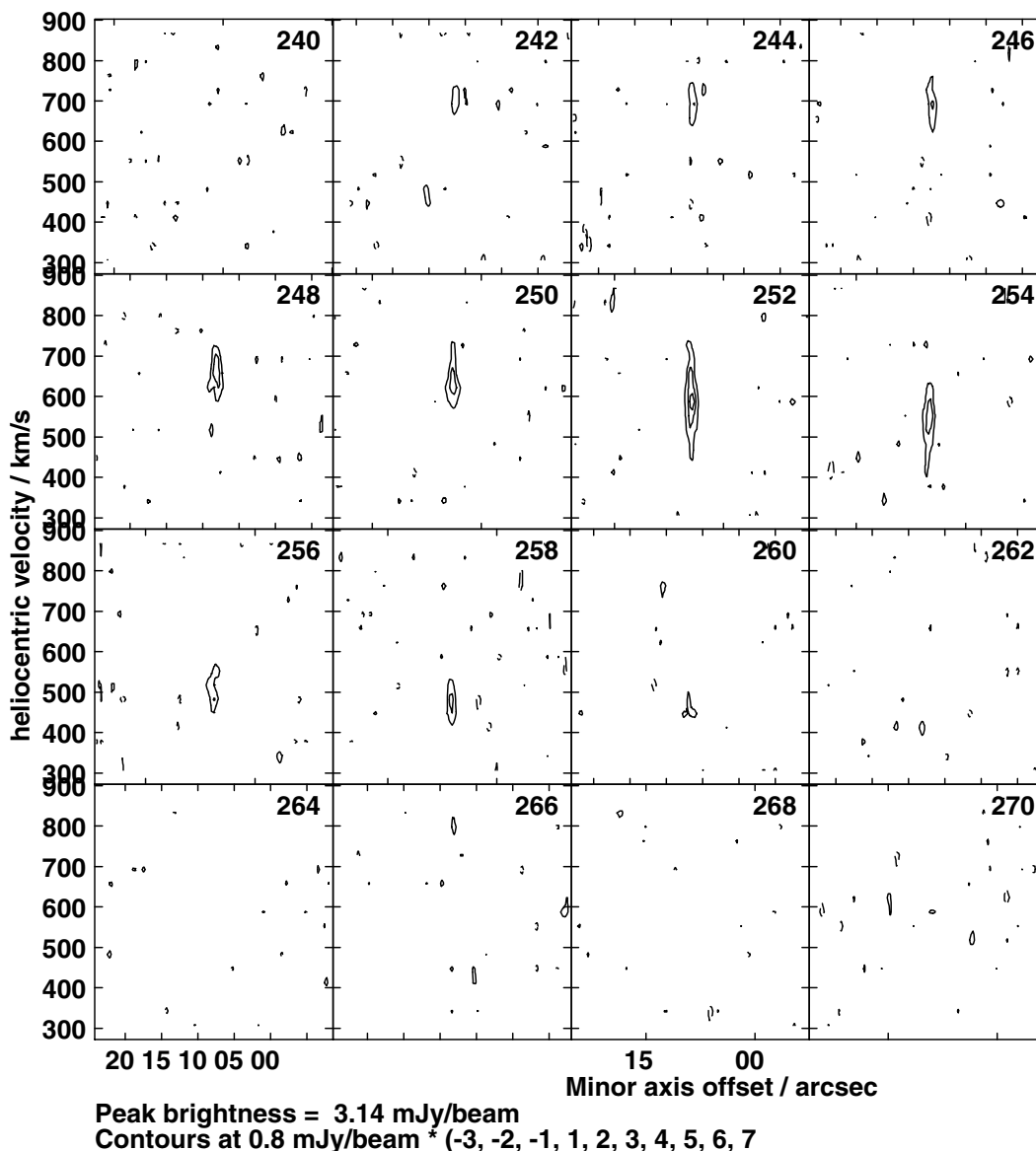


**Fig. 3.** H91 $\alpha$  + H92 $\alpha$  rotation curves along the minor axis direction of the line-emitting region (PA =  $-43^\circ$ ). Each panel is separated by  $0.8''$  along the major axis, with the slice shown in panel 252 passing through the peak of emission at the nucleus. The minor axis offset values are relative to an arbitrary offset. Resolution is  $1.3'' \times 36 \text{ km s}^{-1}$ .

The CO emission seen by both Mauersberger et al. (1996) and Chou et al. (2007) shows two local intensity peaks, with a radius of  $6''$  to  $8''$  from the nucleus. The H91 $\alpha$  + H92 $\alpha$  line emission radial distribution showed a central peak and a ring of emission with radius  $2.5''$  ( $50 \text{ pc}$ ) from the nucleus. Thus, the ring in ionized gas lies within the ring in the molecular gas, consistent with the illustration by Spoon et al. (2003) Fig. 8.

The dynamical mass within the central  $100 \text{ pc}$  radius derived from the CO by Mauersberger et al. (1996) is  $8 \times 10^8 M_\odot$  and the dynamical mass within  $0.3 \text{ pc}$  radius derived from the water masers by Greenhill et al. (1997) is  $1.0 \times 10^6 M_\odot$ . The dynamical mass enclosed within the central  $1''$  ( $19 \text{ pc}$ ) radius derived from the H91 $\alpha$  + H92 $\alpha$  line is  $3 \times 10^7 M_\odot$ , which lies between the masses within the larger and smaller radii, as expected.

Rotation of the nuclear ionized gas is traced also by Pf $\beta$  by Spoon et al. (2003). They find ionized gas within the central  $\pm 5''$  around the nucleus from the same region in which we find H91 $\alpha$  + H92 $\alpha$  emission. Comparing their position-velocity diagram of Pf $\beta$  (their Fig. 7) to our position-velocity diagram of

H91 $\alpha$  + H92 $\alpha$  (our Fig. 2), the diagrams look essentially the same, having the same central velocity gradient, the same rotation rate, the same systemic velocity, and the same overall extent. Thus, both emission lines are tracing the same gas, as expected. Spoon et al. (2003) propose a geometry in which the HI Pf $\beta$  originates from the central ionized and rotating disk (their Fig. 8). The H91 $\alpha$  + H92 $\alpha$  kinematics supports this picture. Similar rotation curves are seen in HCN, HNC, and HCO $^+$  by Cunningham & Whiteoak (2005), though the molecular material is seen more strongly concentrated into an edge-on ring with weak emission or absorption towards the nucleus, unlike the ionized gas which is always in emission.

Chou et al. (2007) identify a kinematically decoupled component in their CO position-velocity diagrams along the minor axis, showing broad velocity width at or near the disk centre, as a strip in velocity at the origin of the position-velocity diagram spanning  $400 \text{ km s}^{-1}$  to  $750 \text{ km s}^{-1}$  in their Fig. 5. They identify this gas as a promising candidate for the circumnuclear molecular torus invoked by AGN unification models. For

comparison, we show the position-velocity diagram in  $H91\alpha + H92\alpha$  along the minor axis in Fig. 3. The  $H91\alpha + H92\alpha$  shows a broad velocity range at the position of the nucleus (panel 252), spanning  $430 \text{ km s}^{-1}$  to  $750 \text{ km s}^{-1}$ , similar to that seen in CO by Chou et al. (2007). This broad velocity width in the centre of our position-velocity diagram along the minor axis underlines that the rotation curve is flat; at this position close to the centre, one sees the full receding and the full approaching velocities, which can be the case only if the rotation curve rises very quickly in the central beam and stays flat further out, as seen the other panels of Fig. 3. The gas with broad velocity width at the nucleus was included when we fit the kinematics and we obtained a good fit with a simple flat rotation curve extending into the central ring; we did not need to introduce any departure from the simple flat-rotation-curve model.

## 7. Conclusions

We have discovered  $H91\alpha + H92\alpha$  lines in emission in NGC 4945 with flux density of  $17.8 \text{ mJy}$  using the ATCA, making NGC 4945 the brightest known extragalactic RRL source. The detected line strength infers an ionized gas mass of  $(2 \text{ to } 6) \times 10^5 M_{\odot}$  and a corresponding star formation rate of  $2 M_{\odot} \text{ yr}^{-1}$  to  $8 M_{\odot} \text{ yr}^{-1}$  depending on the model conditions. The star formation rate estimated from the RRL detection in NGC 4945 agrees well with rates estimated from radio and FIR luminosities using previously-calibrated relations.

The rotation curve was found to be flat into the central  $1''$  with  $v_{\text{systemic}} = 581 \text{ km s}^{-1}$ ,  $v_{\text{rotation}} = 120 \text{ km s}^{-1}$ . We found no need to invoke a bar or radial motion and no indication of a kinematically decoupled component.

Future observations at high frequencies where RRLs are stronger and resolution is higher will provide measurements of multiple transitions to provide better constraints on the gas conditions.

Since RRLs occur over a wide range of wavelengths, a given array can provide higher resolution for studying the dynamics of ionized gas than can be achieved for studies of neutral hydrogen.

Followup with the Atacama Large Millimeter/submillimeter Array of RRLs in NGC 4945 and others should be rewarding, giving good SNR and high spatial resolution to see finer details in the kinematics and of the possible circumnuclear torus.

*Acknowledgements.* The Australia Telescope Compact Array is part of the Australia Telescope, which is funded by the Commonwealth of Australia for operation as a National Facility managed by CSIRO. The National Radio Astronomy Observatory is a facility of the National Science Foundation operated under cooperative agreement by Associated Universities, Inc.

## References

- Ables, J. G., Forster, J. R., Manchester, R. N., et al. 1987, MNRAS, 226, 157  
 Anantharamaiah, K. R., Viallefond, F., Mohan, N. R., Goss, W. M., & Zhao, J. H. 2000, ApJ, 537, 613  
 Baars, J. W. M., Genzel, R., Pauliny-Toth, I. I. K., & Witzel, A. 1977, A&A, 61, 99  
 Batchelor, R. A., Jauncey, D. L., & Whiteoak, J. B. 1982, MNRAS, 200, 19P  
 Chou, R. C. Y., Peck, A. B., Lim, J., et al. 2007, ApJ, 670, 116  
 Cornwell, T. J., Uson, J. M., & Haddad, N. 1992, A&A, 258, 583  
 Cunningham, M. R., & Whiteoak, J. B. 2005, MNRAS, 364, 37  
 Curran, S. J., Johansson, L. E. B., Bergman, P., Heikkilä, A., & Aalto, S. 2001, A&A, 367, 457  
 Dahlem, M., Golla, G., Whiteoak, J. B., et al. 1993, A&A, 270, 29  
 Done, C., Madejski, G. M., & Smith, D. A. 1996, ApJ, 463, L63  
 Dos Santos, P. M., & Lépine, J. R. D. 1979, Nature, 278, 34  
 Elmouttie, M., Haynes, R. F., Jones, K. L., et al. 1997, MNRAS, 284, 830  
 Forbes, D. A., & Norris, R. P. 1998, MNRAS, 300, 757  
 Fukugita, M., & Kawasaki, M. 2003, MNRAS, 340, L7  
 Gardner, F. F., & Whiteoak, J. B. 1974, Nature, 247, 526  
 Greenhill, L. J., Moran, J. M., & Herrnstein, J. R. 1997, ApJ, 481, L23  
 Henkel, C., Whiteoak, J. B., Nyman, L.-Å., & Harju, J. 1990, A&A, 230, L5  
 Henkel, C., Whiteoak, J. B., & Mauersberger, R. 1994, A&A, 284, 17  
 Hopkins, A. M., Miller, C. J., Nichol, R. C., et al. 2003, ApJ, 599, 971  
 Iwasawa, K., Koyama, K., Awaki, H., et al. 1993, ApJ, 409, 155  
 Karachentsev, I. D., Tully, R. B., Dolphin, A., et al. 2007, AJ, 133, 504  
 Kennicutt, R. C. 1989, ApJ, 344, 685  
 Koornneef, J. 1993, ApJ, 403, 581  
 Krabbe, A., Böker, T., & Maiolino, R. 2001, ApJ, 557, 626  
 Lípári, S., Tsvetanov, Z., & Macchetto, F. 1997, ApJS, 111, 369  
 Marconi, A., Oliva, E., van der Werf, P. P., et al. 2000, A&A, 357, 24  
 Mauersberger, R., Henkel, C., Whiteoak, J. B., Chin, Y.-N., & Tieftrunk, A. R. 1996, A&A, 309, 705  
 Mohan, N. R. 2002, Ph.D. Thesis, IISc, Bangalore, India  
 Moorwood, A. F. M., & Oliva, E. 1994, ApJ, 429, 602  
 Moorwood, A. F. M., van der Werf, P. P., Kotilainen, J. K., Marconi, A., & Oliva, E. 1996, A&A, 308, L1  
 Ott, M., Whiteoak, J. B., Henkel, C., & Wielebinski, R. 2001, A&A, 372, 463  
 Paglione, T. A. D., Jackson, J. M., & Ishizuki, S. 1997, ApJ, 484, 656  
 Petrosian, V., Silk, J., & Field, G. B. 1972, ApJ, 177, L69  
 Roy, A. L., Goss, W. M., Mohan, N. R., & Anantharamaiah, K. R. 2005, A&A, 435, 831  
 Roy, A. L., Goss, W. M., & Anantharamaiah, K. R. 2008, A&A, 483, 79  
 Sadler, E. M., Slee, O. B., Reynolds, J. E., & Roy, A. L. 1995, MNRAS, 276, 1373  
 Schurch, N. J., Roberts, T. P., & Warwick, R. S. 2002, MNRAS, 335, 241  
 Spoon, H. W. W., Koornneef, J., Moorwood, A. F. M., Lutz, D., & Tielens, A. G. G. M. 2000, A&A, 357, 898  
 Spoon, H. W. W., Moorwood, A. F. M., Pontoppidan, K. M., et al. 2003, A&A, 402, 499  
 Vacca, W. D., Garmany, C. D., & Shull, J. M. 1996, ApJ, 460, 914  
 Wang, M., Henkel, C., Chin, Y.-N., et al. 2004, A&A, 422, 883  
 Whiteoak, J. B., & Gardner, F. F. 1974, ApJL, 15, 211  
 Whiteoak, J. B., & Gardner, F. F. 1986, MNRAS, 222, 513  
 Whiteoak, J. B., & Wilson, W. E. 1990, MNRAS, 245, 665  
 Whiteoak, J. B., Gardner, F. F., & Høglund, B. 1980, MNRAS, 190, 17P